Comparison of Different Precoding Techniques for Unbalanced Impairments Compensation in Short-Reach DMT Transmission Systems

Ming Chen, *Member, IEEE*, Ling Wang, Dongsheng Xi, Long Zhang, Hui Zhou, and Qinghui Chen

***Abstract*—Channel independent precoding technique has been widely used in optical discrete multi-tone (DMT) transmission systems to compensate unbalanced impairments induced by bandwidth limitations and imperfect frequency responses of electrical/optical devices and various interferences. However, the comparison of different precoding techniques in terms of peak-to-average power ratio (PAPR) reduction, nonlinear distortion tolerance, implementation complexity, and bit error rate (BER) improvements has not been fully studied. In this article, we comparatively investigate seven most commonly used precoding techniques, i.e., discrete Fourier transform (DFT), orthogonal circulant matrix transform (OCT), constant amplitude zero autocorrelation sequence-based matrix transform (CAZACT), Zadoff-Chu matrix transform (ZCT), discrete cosine transform (DCT), discrete Hartley transform (DHT), and Walsh-Hadamard transform (WHT), through both numerical simulations and offline experiments. Simulations show that the ZCT can achieve the best PAPR reduction, and the OCT cannot reduce the PAPR. Besides, DFT, CAZACT, ZCT, DCT, and DHT precoded DMT signals have superior error vector magnitude performance after passing through nonlinear models. And the corresponding precoded QPSK-DMT signals have better BER performance than both OCT/WHT precoded and conventional ones in the distortion-limited scenarios. However, the precoded 16/64QAM-DMT signals, excluding OCT precoded one, are more sensitive to nonlinear distortions and provide minor BER improvement or even may degrade the BER performance. Complexity analysis exhibits the WHT precoding does not require multiplications and therefore has the lowest implementation complexity. In the inter-symbol interference-limited case, OCT precoding can still achieve a good signal-to-noise ratio (SNR) balance and provide the best BER performance. A simple timing synchronization point adjustment (TSPA) method is employed to enhance SNR balance. Simulated and experimental results exhibit that similar BER performance can be achieved by using these precoding techniques together with TSPA in noise-limited scenarios. Considering the implementation complexity, WHT precoding may be a good option to compensate unbalanced impairments in the short-reach DMT transmission system.**

***Index Terms*—Discrete multi-tone, nonlinear distortions, precoding, unbalanced impairments compensation.**

I. Introduction

OPTICAL discrete multi-tone (DMT) is a special direct-detection optical orthogonal frequency-division multiplexing (DDO-OFDM). It has been widely considered as a promising physical-layer technology for future short-reach broadband optical communications due to its inherent advantages, such as high spectral efficiency (SE) and resistance to fiber dispersions. Among DDO-OFDM systems, optical DMT does not require up/down-conversion in the digital or analog domain and has a low implementation complexity. Therefore, it is more suitable for cost-sensitive short-reach applications such as optical access networks [1], [2], optical interconnections in data centers [3], [4], and visible light communications (VLC) [5], [6]. In the literature, numerous field programmable gate array (FPGA) based real-time optical DMT transmission demonstrations have also been reported in [7]–[11].

In an optical DMT system, there several common impairments, such as the imperfect frequency response of optical/electrical devices, chromatic dispersion (CD) induced power fading [12], signal-to-signal beating interference (SSBI) [13] and digital-to-analog converter (DAC) clock tone leakage [14], can lead to the unbalanced signal-to-noise ratio (SNR) distribution over data-carrying subcarriers. We called this phenomenon as unbalanced impairments. As a result, the overall bit error rate (BER) performance may be seriously degraded due to unbalanced impairments. One classical and effective method is to use the adaptive modulation technique, including adaptive power and/or bit loading. And this technique has been widely studied in optical DMT systems to maximize the transmission rate [15], [16]. Meanwhile, a simplified method named pre-emphasis technique is also employed to enhance the transmission performance [17] in the bandwidth-limited system. However, the feedback of the channel state information over all data-carrying subcarriers is required via the reverse link. It is timing consuming. In [13], the authors proposed a static adaptive modulation scheme combined with the forward error correction

Manuscript received May 10, 2020; revised June 29, 2020; accepted July 14, 2020. Date of publication July 17, 2020; date of current version November 16, 2020. This work was supported in part by the National Natural Science Foundation of China under Grant 61805079 and Grant 61701180, in part by the Hunan Provincial Natural Science Foundation of China under Grant 2020JJ4433, and in part by the Scientific Research Fund of the Hunan Provincial Education Department under Grant 18B026 and Grant 18C0520. *(Corresponding author: Ming Chen.)*

Ming Chen, Ling Wang, Dongsheng Xi, and Long Zhang are with the School of Physics and Electronics, Hunan Normal University, Changsha 410081, China (e-mail: ming.chen@hunnu.edu.com; lingwang@smail.hunnu.edu.cn; xds@hunnu.edu.cn; zlong93823@smail.hunnu.edu.cn).

Hui Zhou is with the College of Information Science and Engineering, Hunan Normal University, Changsha 410081, China (e-mail: zhou_zh_hui@hunnu.edu.cn).

Qinghui Chen is with the College of Computer and Communication, Hunan University of Technology, Zhuzhou 412007, China (e-mail: qhchen@hut.edu.cn).

Color versions of one or more of the figures in this article are available online at https://ieeexplore.ieee.org.

Digital Object Identifier 10.1109/JLT.2020.3010002

technique to compensate unbalanced impairments induced by the SSBI and power fading. This scheme may not be suitable for the system with the time-varying channel response.

Recently, channel/signal independent precoding technique has been widely employed in the optical DMT for the compensation of unbalanced impairments [18]–[33]. The idea of precoding is realized by multiplying the quadrature amplitude modulation (QAM) mapped symbols by a precoding matrix in the transmitter. In the receiver side, the QAM symbols are recovered by multiplying the channel equalized data by its inverse matrix. Theoretically, if the amplitudes of the elements in the precoding matrix are equal, then the identical SNR distribution over all of data-carrying after decoding can be achieved [27]. Meanwhile, the precoding may improve the autocorrelation performance of input symbols for the inverse fast Fourier transform (IFFT) function and thus reduce peak-to-average power ratio (PAPR) [28]. Owing to the PAPR reduction, the nonlinear distortions, introduced by optical or electrical devices such as electrical amplifiers, directly modulated lasers (DML) and light-emitting diodes (LED), may be reduced.

In [18], discrete Fourier transform (DFT) precoding technique, also known as DFT-spread, was applied to improve the BER performance of the laser-based short-reach DMT transmission system with a step-index plastic optical fiber link. Besides, DFT precoding is used to improve the BER performance of the optical DMT system with clock tone leakage of DAC and analog-to-digital converters (ADC) [22]. Moreover, a constant amplitude zero autocorrelation sequence based matrix transform (CAZACT) precoding has been proposed to reduce PAPR and balance SNR over data-carrying subcarriers in [23]. The similar PAPR reduction and BER improvement can be achieved by DFT and CAZACT [32]. However, inter-symbol interference (ISI) may degrade the SNR on the edge subcarriers of the DFT and CAZACT-precoded DMT signals. A simplified adaptive modulation scheme with CAZACT precoding was proposed and experimentally demonstrated in [24]. Y. Hong et al. proposed an orthogonal circulant matrix transform (OCT) precoding technique to combat the severe frequency-selective fading of the VLC channel [26]. It indicates that the OCT precoding has better performance in SNR balance than DFT precoding in the bandwidth-limited VLC system [30]. Also, a Zadoff-Chu sequence-based matrix transform (ZCT) has been proposed to reduce the PAPR and up to 3.7 dB PAPR reduction for 1,023 subcarriers can be achieved in a compatible single-sideband DDO-OFDM system [34]. The above mentioned four types of precoding techniques are all realized by using complex-valued precoding matrices. From the perspective of hardware implementation, it is preferred to use the precoding technique with the low complexity for optical fiber communications. In this context, several real-valued matrices based precoding techniques, such as discrete cosine transform (DCT) [35], discrete Hartley transform (DHT) [36] and Wash-Hadamard transform (WHT) [31], are also proposed to reduce PAPR or balance SNR distribution for the optical OFDM transmission system.

Even though the precoding technique has been extensively investigated in the literature, the comparison of different precoding techniques in terms of PAPR reduction, nonlinear distortions tolerance, implementation complexity, and BER improvement has not been fully studied in the optical fiber DMT transmission system. It is interesting to explore which precoding technique is the best choice to compensate unbalanced impairments under different scenarios, such as nonlinear distortion, ISI, and noise limitations. In this paper, we comparatively investigate seven most commonly used precoding techniques, i.e., DFT, OCT, CAZACT, ZCT, DCT, DHT and WHT, for unbalanced impairments compensation in DMT transmission systems by numerical simulations. And a simple timing synchronization point adjustment (TSPA) method is employed to combat ISI to enhance the performance of the precoded DMT without cyclic suffix (CS). Experimental verifications in a DML-based short-reach DMT transmission system are also conducted. Both simulated and experimental results exhibit WHT precoding can achieve similar BER performance in the noise-limited scenario as other precoding techniques, but with the lowest implementation complexity.

The rest of the paper is structured as follows. In Section II, we briefly introduce the working principle of the precoding technique and the construction of different precoding matrices. The analysis of implementation complexity is performed in Section III. The simulation model used in this work is described in Section IV. The PAPR performance of the conventional and the precoded DMT signals are discussed in Section V. The nonlinear distortion tolerance of the precoded DMT signals is investigated with two nonlinear distortion models in Section VI. In Section VII, the BER performance of the precoded DMT signals passing through a bandwidth-limited additive white Gaussian noise (AWGN) channel is measured and discussed. Also, a simple TSPA method for combating ISI and enhancing SNR balance is described in this section. Experimental verification is conducted in Section VIII. Finally, Section IX summarizes the conclusions drawn from this paper.

II. Working Principle of Precoding Technique

In the baseband DMT transmitter, precoding is performed by multiplying the mapped QAM symbols, $\boldsymbol{x} = [x_1, x_2, \ldots, x_M]$, by a precoding matrix, $\boldsymbol{P}$. After this operation, the IFFT is taken to get a real-valued time-domain DMT signal. The precoding matrix $\boldsymbol{P}$ can be expressed as

$$\boldsymbol{P} = \frac{1}{\sqrt{M}} \begin{bmatrix} p_{1,1} & p_{1,2} & \cdots & p_{1,M} \\ p_{2,1} & p_{2,2} & \cdots & p_{2,M} \\ \vdots & \vdots & \ddots & \vdots \\ p_{M,1} & p_{M,2} & \cdots & p_{M,M} \end{bmatrix} \tag{1}$$

where M is the number of data-carrying subcarriers, and $\boldsymbol{P}$ is an orthogonal matrix. And the amplitude of all elements in the precoding matrix $\boldsymbol{P}$ is equal to 1 for DFT, CAZACT, OCT, ZCT, and WHT. In this paper, vectors and matrices are denoted, respectively, with small bold italic letters (e.g., $\boldsymbol{x}$, $\boldsymbol{y}$ and $\boldsymbol{z}$) and capital bold italic letters (e.g., $\boldsymbol{P}$ and $\boldsymbol{H}$). And we use small italic letters with subscript indices (e.g., x_k and $p_{m,n}$) to denote an element of a vector (or a matrix). Besides, scalar constants and scalar variables are denoted with capital italic letters (e.g., M and N) and small italic letters (e.g., n, k and i), respectively.

The precoded symbols $\boldsymbol{y} = [y_1, y_2, \ldots, y_M]$ can be written as

$$\boldsymbol{y}^T = \boldsymbol{P}\boldsymbol{x}^T \tag{2}$$

where $[\cdot]^T$ denotes the matrix transpose. Once the IFFT is done, the precoded DMT signal without cyclic prefix (CP) and CS can be expressed as [37]

$$s(n) = \frac{1}{\sqrt{N}} \sum_{\substack{k=-M \\ k\neq 0}}^{M} y_k \exp\left(j\frac{2\pi kn}{N}\right) \tag{3}$$

where *n* is an integer ranging from 0 to $N-1$, *N* is the IFFT/FFT size, and y_{-k} is the complex conjugate of y_k. In general, the average power of the transmitted QAM symbols, $\boldsymbol{x}$, is usually normalized to unity with the corresponding normalization factor for different QAM modulations (e.g., $\sqrt{2}$ for QPSK and $\sqrt{10}$ for 16QAM). The average power of the precoded symbols after precoding should also be 1. After the $N-$point IFFT operation, the average power of each data-carrying subcarrier is reduced to 1/*N*, according to Eq. (3). And the average power of the precoded DMT signal is 2*M*/*N* because 2*M* of such subcarriers are summed.

A. Precoding Matrices Construction

Different precoding matrices are used to realize DFT, OCT, CAZACT, ZCT, DCT, DHT, and WHT. In DFT precoding, the element of $\boldsymbol{P}$ in the $m-$th row and the $n-$th column is given by

$$p_{m,n}^{DFT} = \exp\left(-j2\pi\frac{(m-1)(n-1)}{M}\right) \tag{4}$$

where *m* and *n* are positive integer numbers ranging from 1 to *M*, and $j = \sqrt{-1}$.

For CAZACT, ZCT, and OCT precoding techniques, a Zadoff-Chu (ZC) sequence with a length of *L* is used to build their precoding matrices with different construction methods. The $k-$th element in the ZC sequence is written as [23]

$$c_k = \begin{cases} \exp\left(j\frac{2\pi r}{L}\left(\frac{(k-1)^2}{2} + q(k-1)\right)\right), L_{\text{even}} \\ \exp\left(j\frac{2\pi r}{L}\left(\frac{k(k-1)}{2} + q(k-1)\right)\right), L_{\text{odd}} \end{cases} \tag{5}$$

where *k* is an integer number ranging from 1 to *L*, *q* is an integer number, *r* is an integer relatively prime to *L* which equals to M^2 for both CAZACT and ZCT, and *M* for OCT, respectively. The corresponding $p_{m,n}$ for the precoding matrices of CAZAT, ZCT, and OCT, are given below.

$$p_{m,n}^{CAZACT} = c_{m+(n-1)M} \tag{6}$$

$$p_{m,n}^{ZCT} = c_{n+(m-1)M} \tag{7}$$

$$p_{m,n}^{OCT} = \begin{cases} c_{n-m+1}, & n-m+1 > 0 \\ c_{n-m+1+M}, & n-m+1 \leq 0 \end{cases} \tag{8}$$

The precoding matrix for ZCT can be constructed by filling the ZC sequence column-wise or row-wise. However, the column-wise filling method may lead to degraded performance in PAPR reduction [38]. In this work, we only investigate the row-wise case for ZCT, unless otherwise stated. CAZACT is a special case of ZCT, and its precoding matrix is filled with the ZC sequence, which is generated with $r = 1$ and $q = 0$, by columns. Whereas, the elements in the $m-$th row of the OCT precoding matrix is the circular shift of the $M-$point ZC sequence by *m*-1 elements [26]. Similarly, the real-valued precoding matrices for DCT and DHT are constructed by

$$p_{m,n}^{DCT} = \begin{cases} 1, & m = 1 \\ \sqrt{2}\cos\left(\frac{\pi(2n-1)(m-1)}{2M}\right), & m \neq 1 \end{cases} \tag{9}$$

$$p_{m,n}^{DHT} = \cos\left(\frac{2\pi mn}{M}\right) + \sin\left(\frac{2\pi mn}{M}\right) \tag{10}$$

Hadamard matrix, whose elements $p_{m,n}^{WHT}$ are either +1 or -1 and whose rows are mutually orthogonal, is used for WHT precoding. The Hadamard matrix of order *M* can be written as

$$\boldsymbol{H}_M = \begin{bmatrix} \boldsymbol{H}_{M/2} & \boldsymbol{H}_{M/2} \\ \boldsymbol{H}_{M/2} & -\boldsymbol{H}_{M/2} \end{bmatrix}, \ \boldsymbol{H}_2 = \begin{bmatrix} 1 & 1 \\ 1 & -1 \end{bmatrix} \tag{11}$$

where $\boldsymbol{H}_2$ is the Hadamard matrices of order 2. If *M* is a power of 2, the $\boldsymbol{H}_M$ can be constructed from $\boldsymbol{H}_2$. Construction methods for other cases can be found in [39]. The corresponding precoding matric is $\boldsymbol{H}_M/\sqrt{M}$ for WHT precoding.

B. SNR Balance

In the DMT receiver, we assume that the timing synchronization is realized ideally, and there are no ISI and inter-carrier interference (ICI). The data vector, for the *M* positive-frequency data-carrying subcarriers $\boldsymbol{z} = [z_1, z_2, \ldots, z_M]$ after $N-$point FFT operation, can be expressed as

$$\boldsymbol{z} = \boldsymbol{H}\boldsymbol{y}^T + \boldsymbol{w}^T \tag{12}$$

where $\boldsymbol{H}$ is the channel response matrix. It is a diagonal matrix denoted by $diag(h_1, h_2, \cdots, h_M)$ and h_k is the channel response of the $k-$th subcarrier. And $\boldsymbol{w} = [w_1, w_2, \ldots, w_M]$ denotes the noise vector in the frequency domain. We assume that w_k obeys Gaussian distribution with zero mean and variance σ_k^2.

We also suppose the ideal channel estimation is obtained. The recovered QAM symbols, $\hat{x} = [\hat{x}_1, \hat{x}_2, \cdots, \hat{x}_M]$, after channel equalization and decoding can be given by

$$\begin{aligned} \hat{\boldsymbol{x}}^T &= \boldsymbol{P}^{-1}\boldsymbol{H}^{-1}\boldsymbol{z} \\ &= \boldsymbol{x}^T + \boldsymbol{P}^{-1}\boldsymbol{H}^{-1}\boldsymbol{w}^T \\ &= \boldsymbol{x}^T + \bar{\boldsymbol{w}}^T \end{aligned} \tag{13}$$

where $\boldsymbol{P}^{-1}$ and $\boldsymbol{H}^{-1} = diag(1/h_1, 1/h_2, \ldots, 1/h_M)$ denote the inverse matrices of $\boldsymbol{P}$ and $\boldsymbol{H}$, respectively. Note that $\boldsymbol{P}$ is the orthogonal matrix and its inverse matrix $\boldsymbol{P}^{-1}$ equals to the conjugate transpose of $\boldsymbol{P}$. Thus, the noise item $\bar{\boldsymbol{w}}^T$ in Eq. (13) can be further expanded to

$$\bar{\boldsymbol{w}}^T = \boldsymbol{P}^{-1}\boldsymbol{H}^{-1}\boldsymbol{w}^T$$

$$= \frac{1}{\sqrt{M}} \begin{bmatrix} p_{1,1}^* & p_{2,1}^* & \cdots & p_{M,1}^* \\ p_{1,2}^* & p_{2,2}^* & \cdots & p_{M,2}^* \\ \vdots & \vdots & \ddots & \vdots \\ p_{1,M}^* & p_{2,M}^* & \cdots & p_{M,M}^* \end{bmatrix}$$

$$\times \begin{bmatrix} \frac{1}{h_1} & 0 & \cdots & 0 \\ 0 & \frac{1}{h_2} & \cdots & 0 \\ \vdots & \vdots & \ddots & \vdots \\ 0 & 0 & \cdots & \frac{1}{h_M} \end{bmatrix} \begin{bmatrix} w_1 \\ w_2 \\ \vdots \\ w_M \end{bmatrix}$$

$$= \frac{1}{\sqrt{M}} \begin{bmatrix} \frac{p_{1,1}^* w_1}{h_1} + \frac{p_{2,1}^* w_2}{h_2} + \cdots + \frac{p_{M,1}^* w_M}{h_M} \\ \frac{p_{1,2}^* w_1}{h_1} + \frac{p_{2,2}^* w_2}{h_2} + \cdots + \frac{p_{M,2}^* w_M}{h_M} \\ \vdots \\ \frac{p_{1,M}^* w_1}{h_1} + \frac{p_{2,M}^* w_2}{h_2} + \cdots + \frac{p_{M,M}^* w_M}{h_M} \end{bmatrix}$$

$$= \frac{1}{\sqrt{M}} \left[\sum_{i=1}^{M} \frac{p_{i,1}^* w_i}{h_i}, \sum_{i=1}^{M} \frac{p_{i,2}^* w_i}{h_i}, \cdots, \sum_{i=1}^{M} \frac{p_{i,M}^* w_i}{h_i} \right]^T$$

$$= [\bar{w}_1, \bar{w}_2, \cdots, \bar{w}_M]^T \tag{14}$$

where $[\cdot]^*$ denotes the complex conjugate, $\bar{w}_k$ represents the noise on the $k-$th subcarrier after decoding. Here, we treat it as an Gaussian noise with zero mean and variance $\bar{\sigma}_k^2$which can be expressed as

$$\bar{\sigma}_k^2 = \frac{1}{M} \sum_{i=1}^{M} \sigma_i^2 \left| \frac{p_{i,k}^*}{h_i} \right|^2 \tag{15}$$

As discussed on Eq. (3) and the average power of the transmitted QAM symbols $\boldsymbol{x}$ is normalized to 1. Thus, the SNR of the $k-$th data-carrying subcarrier can be defined as

$$\gamma_k = \frac{1}{\bar{\sigma}_k^2} = \frac{M}{\sum_{i=1}^{M} \sigma_i^2 \left| \frac{p_{i,k}^*}{h_i} \right|^2} \tag{16}$$

We know that the amplitude of elements in the precoding matrices is identical, i.e., $|p_{i,k}^*| = 1$, for DFT, CAZACT, OCT, ZCT, and WHT. Therefore, the ideal SNR balance can be achieved with these five precoding techniques. However, the SNR balance performance of DCT and DHT precoding techniques will depend on channel response and noise distribution. This is due to the unequal amplitude of elements in the precoding matrices. We will further discuss this problem in the sections of numerical simulation and offline experiments.

The conventional DMT can also be regarded as a special precoded DMT with a unit or identity precoding matrix. The corresponding SNR can be derived from Eq. (16) and given by

$$\gamma_k' = \frac{|h_k|^2}{\sigma_k^2} \tag{17}$$

III. Complexity Comparison

The implementation complexity, according to Eq. (2) and of the corresponding possible fast algorithms is analyzed. The required real multiplications and additions are listed in Table I. A straightforward implementation of precoding techniques may be very resource-intensive. These precoding techniques can be implemented with their fast algorithms by exploiting DFT [30], [40], [41]. It turns out that a significant reduction in implementation complexity is achieved. When M is a power of 2, the implementation complexity of the fast algorithms for the six precoding is given in Table I. Note that the complexity of real-valued DCT was presented in [40]. However, the complex-valued QAM symbols are used in this research. The real parts and image parts of QAM symbols can be transformed independently using two real-valued DCT functions. Therefore its complexity will be doubled. According to [41], the fast real-valued DHT can be realized by simply subtracting the imaginary from the real portion of the DFT of a real-valued sequence. It requires the same multiplications and $M-2$ more additions than the real-valued DFT. Similarly, the fast complex-valued DHT will be implemented with the same multiplications and $2M-4$ more additions than the complex-valued DFT. While the complexity of fast algorithms for CAZACT, OCT and ZCT is the same and equivalent to one $M-$point complex-valued DFT and two $M-$point complex-valued multiplications [30]. The multiplications and additions as a function of data-carrying subcarriers M for their fast algorithms and WHT precoding are also shown in Fig. 1(a) and (b), respectively. It shows that complex-valued OCT, CAZACT, and ZCT precoding techniques require more multiplications than real-valued DCT, DFT and DHT precoding ones. And similar additions are needed for the precoding techniques except for WHT. More additions but no multiplications are required for the implementation of WHT precoding. Pipeline multipliers are required for high-speed optical communications and more resource intensive than adders. Therefore, WHT precoding has the lowest complexity.

TABLE I
Implementation Complexity Comparison

Precoding	Refer to Eq. (2)		Fast algorithm	
	Mult	Add	Mult	Add
DFT	$4M^2$	$4M^2$-$2M$	$M\log_2(M)$-$3M$+4	$3M\log_2(M)$-$3M$+4
CAZACT/ ZCT/OCT			$M\log_2(M)$+$5M$+4	$3M\log_2(M)$+M+4
DCT	$2M^2$	$2M^2$-$2M$	$M\log_2(M)$	$3M\log_2(M)$-$2M$+2
DHT			$M\log_2(M)$-$3M$+4	$3M\log_2(M)$-M
WHT	0	$2M^2$-$2M$	-	-

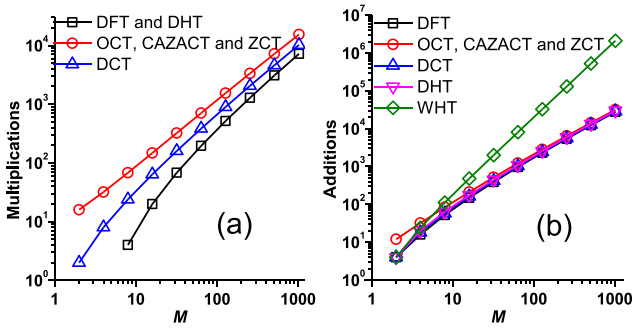

Fig. 1. The required real (a) multiplications and (b) additions versus data-carrying subcarriers M for different precoding techniques.

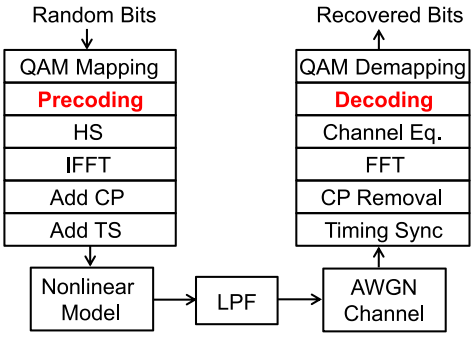

Fig. 2. The block diagram of simulation model.

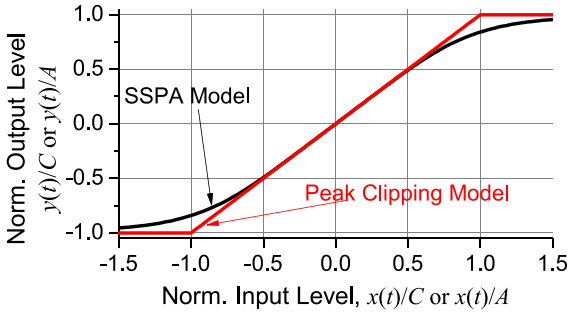

Fig. 3. The normalized transfer function of two nonlinear models.

IV. Simulation Model

In the numerical simulation, a DMT transmission system model with nonlinear distortion, bandwidth limitation and Gaussian noise is established, as depicted in Fig. 2. The random binary bits are first mapped to QAM symbols and followed by precoding. And the precoded symbols are constrained to have Hermitian symmetry (HS) to offer a real-valued time-domain signal after IFFT operation. Afterward, a CP is inserted in front of each IFFT output to combat the ISI caused by the bandwidth limitation. Besides, a training symbol (TS) is also added for each DMT frame to realize both timing synchronization and channel equalization [9]. In this work, the IFFT size (N), CP and CS lengths are 1024, 32 and 0, respectively. Among 1024 subcarriers, direct current (DC) subcarrier is reserved, 768 low-frequency subcarriers are used for data transmission and other high-frequency subcarriers are filled with zeros to achieve an oversampling factor of 1.33. Three QAM modulation formats, i.e., 4, 16 and 64QAM, are discussed. There are one TS and 1,000 DMT symbols in each DMT frame.

Two types of nonlinear distortion models are considered. One is the well-known peak clipping model and its transfer function for the DMT signal can be described by

$$y\left(t\right)=\begin{cases} x\left(t\right), & \left|x\left(t\right)\right|<C \\ \mathrm{sgn}\left(x\left(t\right)\right)\cdot C, & \left|x\left(t\right)\right|\geq C \end{cases} \tag{18}$$

where C is the clipping threshold value, and $sgn(\cdot)$ represents the sign function. The normalized transfer function curve is given in Fig. 3. Here, the clipping ratio (CR) in decibel is defined as [9]

$$CR_{dB}=20\cdot\log_{10}\left(C/rms\left[s\left(n\right)\right]\right) \tag{19}$$

where $rms[s(n)]$ denotes the root mean square of the DMT signal $s(n)$.

The other is a simple solid-state power amplifier (SSPA) model. The transfer function of SSPA can be defined as [42]

$$y\ \left(t\right)=\frac{g_0\cdot A\cdot\mathrm{sgn}\left(x\left(t\right)\right)}{\left(1+\left(A/\left|x\left(t\right)\right|\right)^{s}\right)^{1/s}} \tag{20}$$

where g_0 is the amplifier gain, A denotes the limited level or the input saturation amplitude, and the parameter S controls the sharpness of the saturation region. The input and output levels are $x(t)$ and $y(t)$, respectively. We take $S=4$ in our simulation as a good approximation of the commercial amplifiers [43]. The normalized transfer function curve is also plotted in Fig. 3.

In the simulation, unbalanced impairments are emulated by a 3rd order finite impulse response (FIR) low-pass filter (LPF). The frequency response as a function of the normalized frequency is shown in Fig. 4. The maximum positive-frequency subcarrier index of the DMT signal is 384. The corresponding normalized frequency is 0.75. Therefore the power fading over the data-carrying subcarriers can be up to about 20 dB after the LPF. The average power of the $k-$th data-carrying subcarrier of the filtered signal will be $|h_k|^2/N$, according to the discussion of Eq. (3). Once the filtered DMT signal passes through an AWGN channel and the noise is evenly distributed to all N subcarriers, the unbalanced SNR over data-carrying subcarriers will be observed. If no nonlinear distortions are considered, then the noise power σ^2 on each subcarrier before $N-$point FFT operation can be written as

$$\sigma^2=\frac{2\sum_{i=1}^{M}\left|h_i\right|^2\Big/N}{\gamma N}=\frac{2\sum_{i=1}^{M}\left|h_i\right|^2}{\gamma N^2} \tag{21}$$

where γ is the SNR of the AWGN channel. The noise power after $N-$point FFT operation, i.e., σ_k^2, on each subcarrier is also identical and equal to $N\sigma^2$, according to the definition of FFT in [37]. Subsequently, the noise power σ_k^2 can be substituted into Eqs. (16) and (17) to obtain the SNR on the each data-carrying subcarrier for the precoded DMT signals and the conventional signals, respectively.

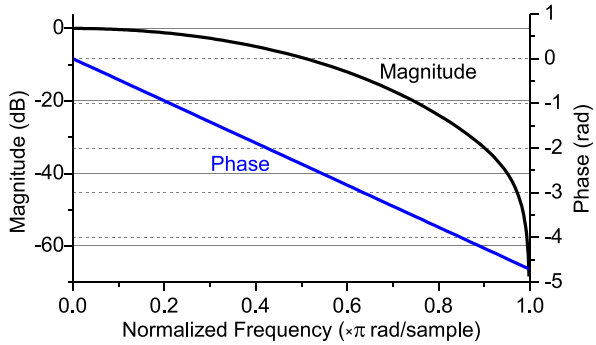

Fig. 4. The frequency response of the 3rd order FIR LPF.

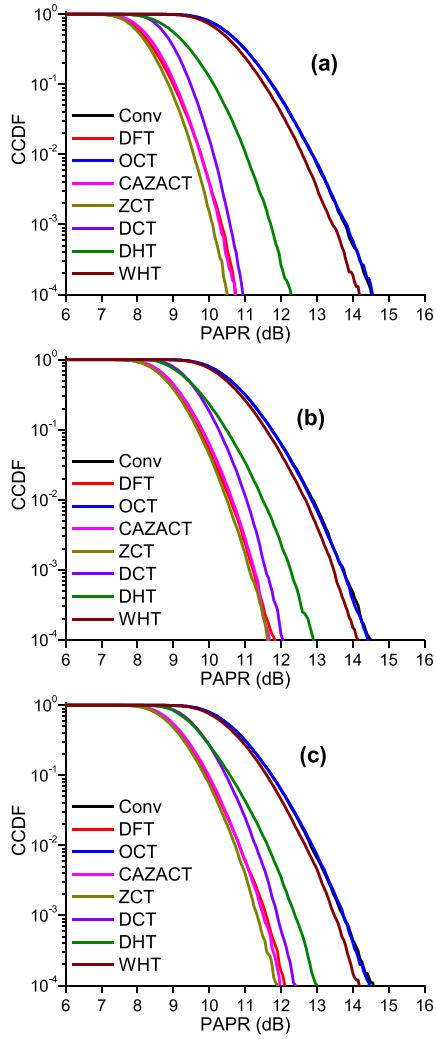

Fig. 5. The PAPR of different precoded DMT signals with (a) QPSK, (b) 16 QAM and (c) 64 QAM mapping.

In this paper, we define the error vector magnitude (EVM) in decibel as

$$EVM_{dB} = 20 \cdot \log_{10}\left(\sqrt{\sum_{k=1}^{K}|e_k|^2 \Big/ \sum_{k=1}^{K}|x_k|^2}\right) \qquad (22)$$

where $x_k$denotes the reference QAM symbol, $\hat{x}_k$is the recovered version, K is the total number of the transmitted QAM symbols and $e_k = \hat{x}_k - x_k$ is the error signal. In this work, $K = 1{,}000 \times M = 384{,}000$.

V. PAPR of the Precoded DMT Signals

The PAPR reduction performance of different precoding techniques is investigated by numerical simulations. The complementary cumulative distribution function (CCDF) as a function of PAPR for the precoded DMT signals is shown in Fig. 5. Each CCDF curve is calculated from 100,000 DMT symbols. And three QAM modulation formats, i.e., QPSK, 16QAM and 64QAM, are discussed. The corresponding CCDF curves are presented in Fig. 5(a), (b), and (c), respectively. Note that M is 384, and r and q for the CAZAC sequence generation are 1 and 0 [23], [24], respectively. The precoding matrices for OCT and ZCT are generated with $r = 11$ and $q = 1$. We can see that the ZCT precoding offers superior PAPR reduction capability, and a similar PAPR performance can be observed for CAZACT and DFT precoding techniques. Besides, OCT precoding has no ability to reduce the PAPR. At a CCDF of 1e-3, the PAPRs of the QPSK-DMT signals with ZCT, DFT, CAZACT, DCT, DHT, and WHT precoding techniques can be reduced by 3.7, 3.5, 3.5, 3.2, 2.1 and 0.4 dB, respectively, compared to the conventional DMT signal. However, we also observe that the PAPR performance with precoding is degraded for higher-order modulation formats. And there are only 2.7 and 2.5 dB PAPR reductions with ZCT precoding, at the CCDF of 1e-3, for 16QAM and 64QAM, respectively. It is concluded from Fig. 5 that the PAPR of the precoded DMT signals, except for OCT and WHT cases, is sensitive to QAM modulation formats. The PAPR of the precoded DMT signals increases with the order of modulation format. One possible reason for this phenomenon is that the high-order QAM symbols have higher PAPRs than that of the low-order ones.

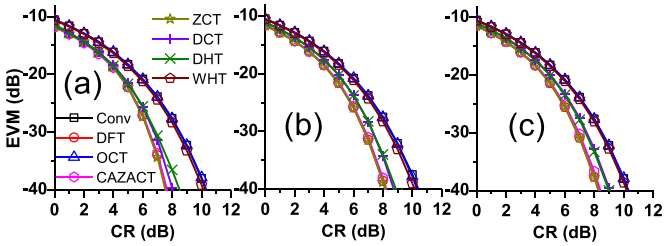

Fig. 6. The EVM performance versus CR using peak clipping model: (a) QPSK, (b) 16QAM and (c) 64QAM.

VI. Nonlinear Distortions

It is interesting to explore the impacts of nonlinear distortions on the precoded DMT transmission system. Firstly, we measure the EVM performance under the different CRs using the peak clipping model, as shown in Fig. 6. It seems that better EVM performance is obtained with larger PAPR reduction after peak clipping. A similar EVM performance is observed for ZCT, DFT, and CAZACT precoding techniques. There is no difference in EVM performance between the OCT precoded DMT signal and the conventional DMT signal. The EVM performance is slightly improved by using WHT precoding due to its low PAPR reduction. It also exhibits that the DHT precoded DMT signal is more sensitive to clipping noise than the DCT precoded one. Although there is a difference in PAPR between DCT and DHT precoding, a similar EVM performance can be found, especially for the 16QAM and 64QAM modulation formats.

The BER performance as a function of CR for the three modulation formats is also investigated and presented in Fig. 7. With QPSK modulation format, DHT precoding outperforms other precoding techniques in combating clipping distortions. An improvement in BER performance can be achieved with precoding techniques, except for WHT and OCT precoding techniques. Besides, a slight BER performance degradation

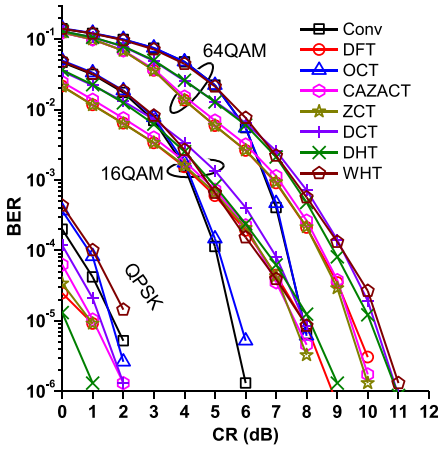

Fig. 7. The measured BER performance versus CR using peak clipping model.

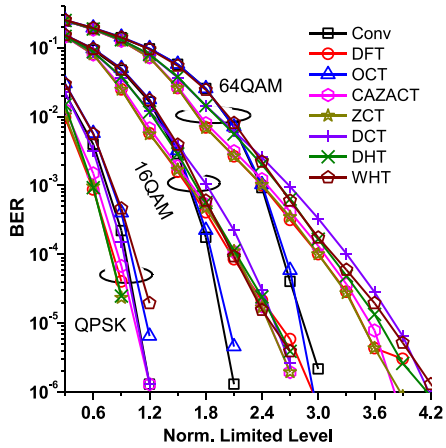

Fig. 9. The measured BER performance versus normalized limited level using SSPA model.

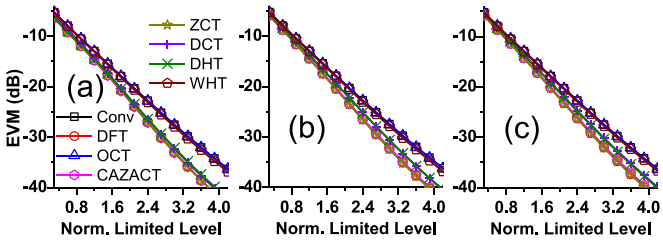

Fig. 8. The EVM performance versus the normalized limited level using SSPA model: (a) QPSK, (b) 16QAM and (c) 64QAM.

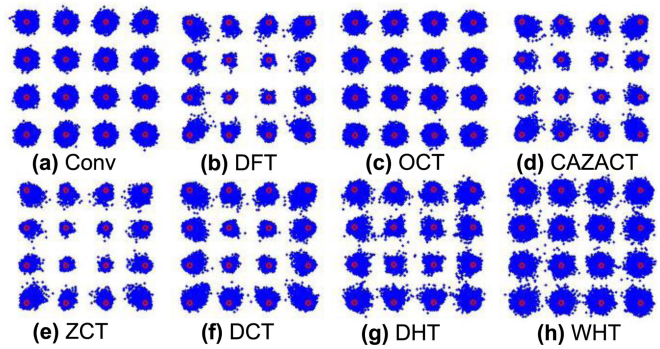

Fig. 10. The recovered 16QAM constellation diagrams ($A_{norm} = 2.4$). The ideal constellation points are marked with red circles.

is also observed for WHT precoding. However, the precoded DMT signals with 16QAM and 64QAM modulation formats, except for the OCT precoding, are more sensitive to the peak clipping at the large CR. The BER performance of the precoded 16/64QAM-DMT signals, with a CR of larger than 4/6.5 dB, is worse than that of the conventional and OCT precoded DMT signals. The improvement in the BER performance is obtained by using precoding techniques, excluding WHT, only when the 16/64QAM-DMT signals suffer heavy clipping distortions.

Similarly, we also investigate the EVM and BER performances of the precoded DMT signals using the SSPA model. Instead of changing the amplitude of the signal, we adjust the limited level A of the SSPA model to explore the effect of different nonlinear distortions on the precoded signals. We define the normalized limited level as $A_{norm} = A/rms[s(n)]$. The corresponding EVM and BER results are shown in Figs. 8 and 9, respectively.

As we can see from the EVM and BER performance curves, similar conclusions can be obtained for the SSPA model, compared to the peaking clipping model. OCT precoded signals have the same EVM and BER performances as the conventional DMT signals with different modulation formats. Precoding techniques may be employed to combat severe nonlinear distortions and improve the BER performance except for OCT and WHT cases. However, the BER performance of the precoded DMT signals with high-level modulation formats, excluding OCT, are more sensitive to the nonlinear distortion. It leads to the degraded BER performance under relatively low nonlinear distortions. Note that we only discuss the effects of the nonlinear distortions on the performance of the DMT signals without taking other factors (e.g., noises and bandwidth limitations) to account. It does not mean the conventional and OCT-precoded DMT systems always outperforms the other precoded DMT ones suffering noises or/and other impairments under relatively low nonlinear distortions. We will discuss this point in detail in Section VII.

In an SSPA model with a normalized limited level of 2.4, the recovered constellation diagrams are plotted in Fig. 10. Although there is an improvement in EVM performance by using precoding techniques except for OCT, a small number of recovered 16QAM symbols show a more significant deviation from their ideal constellation points than that of the conventional one. This case may lead to the degraded BER performance in nonlinear distortion-limited high-order QAM encoded DMT systems. However, the QPSK modulation format, with larger minimum Euclidean distance (MED), is less sensitive to the nonlinear distortion. And the BER performance of the QPSK-DMT system with distortion limitations can be improved by using DFT, CAZACT, ZCT, DCT, and DHT precoding techniques.

VII. Unbalanced Impairments Compensation

In this section, we first discuss the unbalanced impairments emulated by an LPF with high power fading in the high-frequency subcarriers. This phenomenon often can

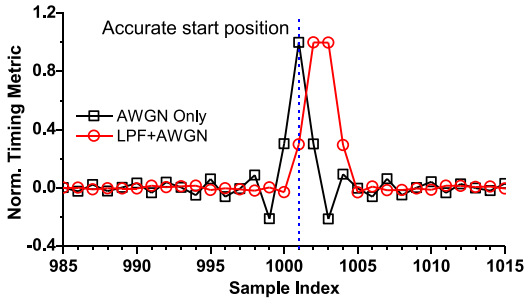

Fig. 11. The normalized timing metric versus sample index (SNR = 30 dB).

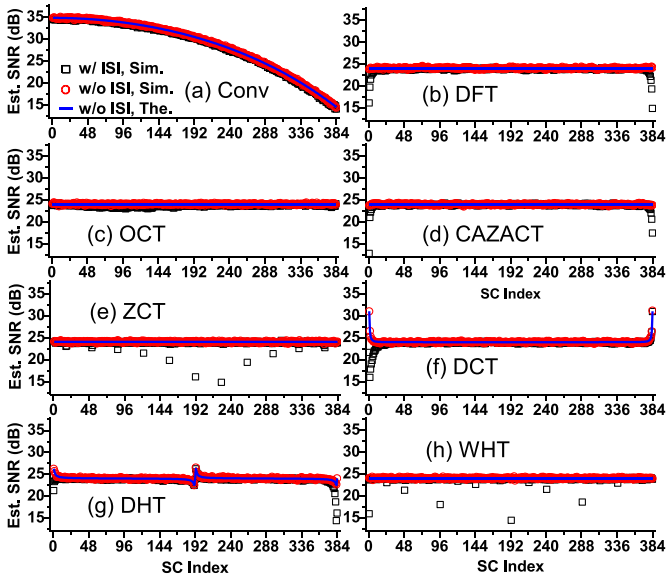

Fig. 12. The estimated SNR over different data-carrying subcarriers for w/ and w/o ISI cases (SNR = 30 dB).

be found in the bandwidth-limited optical/electrical devices (e.g., DAC, DML and LED) and CD-induced frequency selective power fading. The low-pass filtering effect may degrade the performance of the TS-based autocorrelation timing synchronization [9], which may lead to ISI if no CS is applied. Fig. 11 shows the normalized timing metrics of the timing synchronization where two cases, i.e., only the AWGN channel and LPF+AWGN channel, are considered.

The accurate start position of the DMT frame is at the sample index of 1001 in our simulation. It can be accurately estimated under AWGN channel. However, there two similar peaks at sample indices of 1002 and 1003 can be observed for the LPF+AWGN case. This inaccurate timing synchronization will lead to ISI and degrade the SNR balance after precoding. Note that sampling clock phase offsets (SCPO) between DAC and ADC will also influence the timing performance, and a similar timing metric can also be obtained as presented in our previous works [9], [44]. The SNR as a function of the subcarrier index is estimated for different precoding techniques in the presence/absence of ISI, as shown in Fig. 12. Here, the SNR of the AWGN channel is set as 30 dB. Note that no nonlinear distortions are considered, and zero-forcing channel equalization is performed with accurate channel estimation from the channel response of LPF. Also, we calculate the corresponding theoretical SNR in the absence of ISI, according to Eqs. (16), (17) and (21). The estimated SNR distributions for different precoding techniques agree well with theoretical ones. The unbalanced SNR distributions for DHT and DCT precoding techniques are attributed to their precoding matrices which consist of elements with unequal amplitudes. It should be noted that the estimated average SNR values of all precoded signals are identical to about 24 dB. Therefore, high SNRs on the edge subcarriers can be observed for the DCT precoding, but SNRs on the other subcarriers are slightly degraded.

In the presence of ISI, the overall SNR performance of the conventional DMT signal is only slightly degraded, which is benefited from the use of large-size FFT. In [21], it exhibits that large-size FFT can be used to combat ISI more effectively. The identical average SNR values of 23.7 dB can also be obtained for both the conventional DMT and precoded ones. However, the behaviors of SNR distribution on the data-carrying subcarriers are, to some extent, different even if the precoding matrices consist of elements with equal amplitudes. Among precoding techniques, OCT precoding shows good robustness against ISI and achieves the best SNR balance. As we can see from Fig. 12(c), slight SNR degradation occurs on the tens of consecutive subcarriers. However, severe SNR degradation centrally occurs on a small number of subcarriers for other precoding techniques. In the literature, we can find similar situations in [24]–[26]. In this case, the BER performance of the precoded DMT transmission system may be limited by the ISI. One may use CS to combat this type of ISI [30], however, which results in reduced SE. Alternatively, an accurate timing synchronization method, which is robust against the low-pass filtering effect and SCPO, can be employed to avoid the effect of ISI on the precoding. In this paper, we use a simple TSPA method to reduce the effect of ISI on the SNR balance performance of the precoded DMT signals. By using TSPA, the final estimated start point of the DMT frame is adjusted to $d_{max} - Q$, where Q is a non-zero positive integer and d_{max} is the sample index when the timing metric is maximized. As we can see from Fig. 11, the Q value can be set to 2, which is enough to combat this type of ISI.

We also investigate the BER performance of the precoded signals which suffer from both nonlinear distortions and low-pass filtering in an AWGN channel. Here, we use the SSPA model with a normalized limited level of 4.2. Intra-symbol frequency averaging method [45] is employed to enhance the accuracy of channel estimation. The BER performance as a function of SNR ranging from 10 to 40 dB is depicted in Fig. 13. As we can see from Fig. 11, the estimated start position of the DMT frame with TS maybe 1002 or 1003. Here, we fix it at 1002 to keep the consistency under different SNRs. We investigate the BER performance under two cases, i.e., without TSPA and with TSPA, and the corresponding results are presented in Fig. 13(a) and (b), respectively.

In general, the BER performance can be improved by using the precoding technique. However, it may be limited by the ISI. Fig. 13(a) exhibits that OCT precoding with high-order modulation formats can achieve the best BER performance than other precoding techniques. This fact is due to its more rubout against the ISI. Also, similar BER performance can be observed

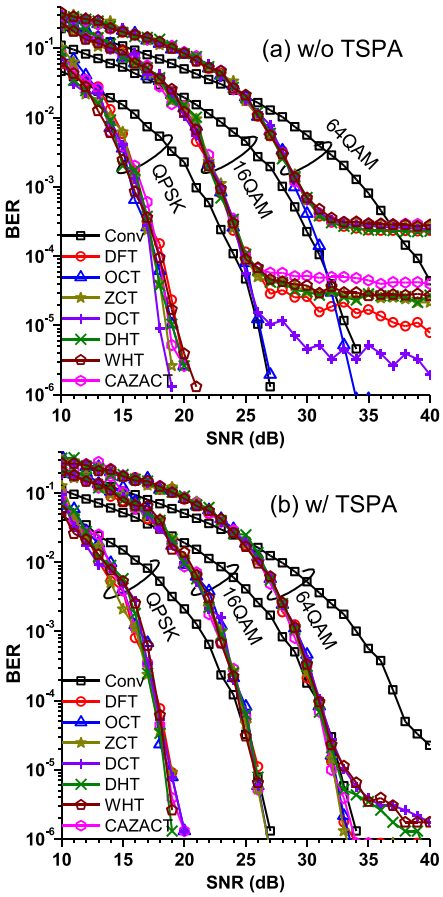

Fig. 13. The measured BER performance versus SNR: (a) w/o TSPA and (b) w/ TSPA.

for the precoded signal with QPSK modulation format due to its large MED. Furthermore, there are slight degradations in the BER performance in relative low SNRs for both w/o TSPA and w/ TSPA cases, compared to the conventional one. One possible reason may be the large SNR difference over data-carrying subcarriers before precoding. By using the TSPA method, the BER performance of the precoded signals can be obviously improved under high SNRs, as shown in Fig. 13(b). We also observe the error floor in BER performance for the three real-valued precoding techniques due to nonlinear distortions.

VIII. Experimental Verifications

A proof-of-concept short-reach optical DMT transmission experiment is conducted to fully investigate the performance of different precoding techniques. The block diagram of the experimental setup is illustrated in Fig. 14. In the transmitter, the digital DMT signals are generated offline using the same DSP algorithms and parameters as simulations and uploaded to a Tektronix arbitrary waveform generator (AWG, AWG7122C) operating at 10-bit resolution and the sampling rate of 12 GSa/s. It should be pointed out that the average power of the precoded DMT signals and the conventional signal remains the same by inserting the same peak amplitude in front of TS in our experiment. The high-frequency image of the converted

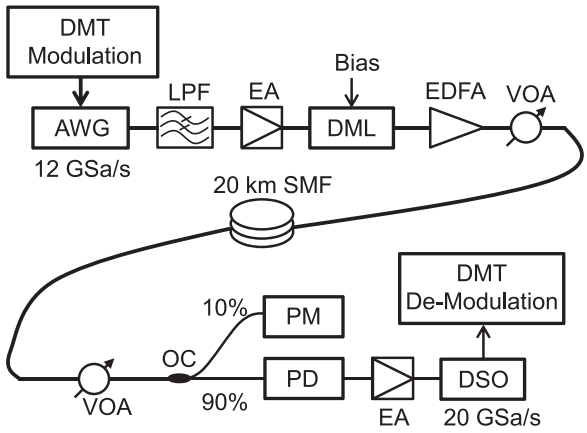

Fig. 14. Experimental setup.

signal is suppressed by an LPF. A 14 GHz electrical amplifier (EA, Mini-Circuit ZX60-14012L-S+) is employed to boost the filtered signal and drives a low-cost 10 Gbit/s DML (NEL, NLK1551SSC) biased at its optimal linear regime. The central wavelength and optical power of the optical DMT signal are 1558 nm and 2.3 dBm, respectively. An erbium-doped fiber amplifier (EDFA) manufactured by Amonics and followed by a variable optical attenuator (VOA) is used to adjust the launch power. The maximum output power of the EDFA is about 13 dBm, and the insertion loss of VOA is about 1 dB. Therefore, the maximum launch power in our experiment is 12 dBm. It should be noted that the launch power can also be tuned by adjusting the pump current of the EDFA. However, the greater noise figure (NF) can be found in [46] when the pump power is relatively low. Therefore, we use the VOA to change the launch power and maintain the same NF for different launch powers. After 20 km of single-mode fiber (SMF) transmission, the second VOA and an optical coupler (OC) placed in front of a 10 GHz photodiode (PD) and a power meter (PM) to change and measure the received optical power (ROP) simultaneously. The power ratio of the OC is 9:1. The recovered signal is amplified by the second EA and captured by a Lecory digital storage oscilloscope (DSO, Wavemaster 820Zi-A). The analog bandwidth, vertical resolution, and maximum sampling rate are 20 GHz, 8-bit, and 40 GSa/s, respectively. The sampling rate is set to 20 GSa/s in our experiment. The captured samples are stored and resampled to 12 GSa/s. The following data processing procedure is shown in Fig. 2.

The estimated SNR from the recovered QPSK symbols after 20 km SMF transmission as a function of the subcarrier (SC) index is presented in Fig. 15. The peak-to-peak voltage (Vpp) of the output signal from the AWG is set to 500 mV. There are unbalanced impairments over data-carrying subcarriers of the conventional DMT signal. Low SNRs can be found on both low- and high-frequency subcarriers. The imperfect frequency response of the DML is the main reason for low SNRs on the subcarriers around DC. The degraded SNR on the high-frequency subcarriers is mainly attributed to the bandwidth limitations of AWG and DML, and CD-induced power fading. Even though the bandwidth of DMT signals and the transmission distance are

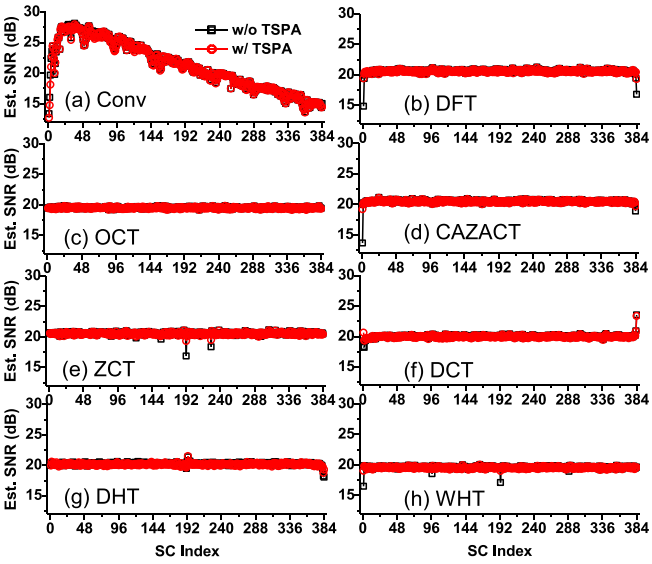

Fig. 15. The estimated SNR versus subcarrier (SC) index for different DMT signals. (Vpp = 500 mV, ROP = 0 dBm and LP = 6 dBm).

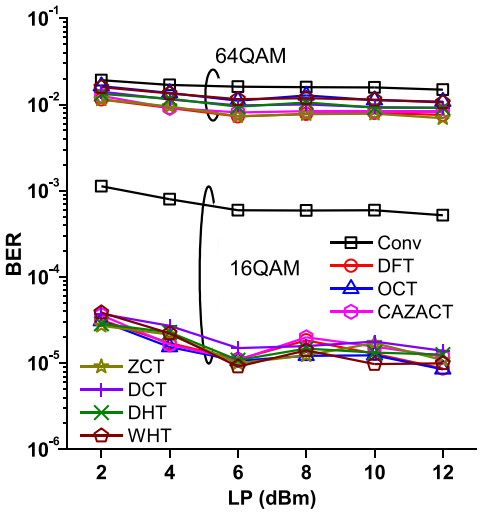

Fig. 16. The measured BER performance versus LP. (Vpp = 500 mV and ROP = 0 dBm).

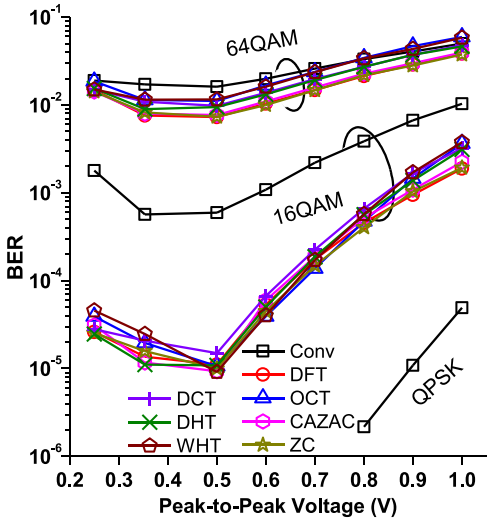

Fig. 17. The measured BER performance with different signal Vpp. (LP = 6 dBm and ROP = 0 dBm).

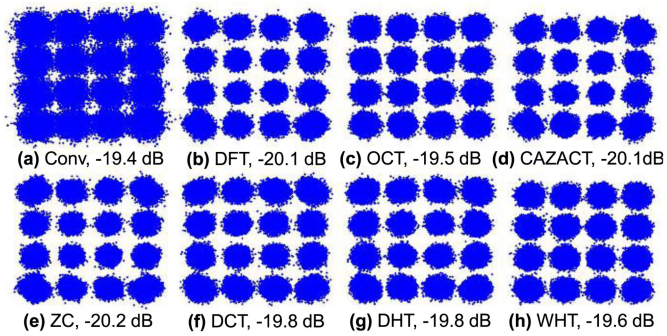

Fig. 18. The recovered 16QAM constellation diagrams and the corresponding EVM values. (Vpp = 500 mV, LP = 6 dBm and ROP = 0 dBm).

only 4.5 GHz and 20 km, respectively, the CD-induced power fading is intensified after fiber transmission due to the strong positive transient chirp of the DML [47], [48]. The effect of ISI on the conventional DMT signal with large-size FFT is ignored. It further indicates that the SNR balance of the precoding techniques can be enhanced by employing the proposed simple TSPA method. Only the case of with TSPA is considered in the following discussions.

We adjust the launch power (LP) to investigate the effect of optical fiber nonlinearity on the BER performance. The related results are shown in Fig. 16. The signal Vpp is set to 500 mV and ROP is fixed at 0 dBm for the BER measurements when LP is higher than 6 dBm. Due to the fiber attenuation and insertion losses of OC and two VOAs, the corresponding ROP is less than 0 dBm when LP is set to 2 or 4 dBm. This leads to slight BER performance degradation. We also can see that the nonlinear effect induced by the optical fiber is small and can be ignored even though the LP is set up to 12 dBm. The error-free transmission is observed for the QPSK modulation format. And the BER performance of the 16QAM-DMT signal can be improved by more than one order of magnitude by using precoding techniques, compared to the conventional DMT case. According to the relationship between BER and SNR, the required SNR is 19.8 dB when the desired BER is 1e-2 for 64QAM modulation format [15]. The measured BER of the precoded 64QAM-DMT signals is well consistent with the theoretical value. The slight BER improvement is obtained after precoding for 64QAM modulation. This fact is mainly due to the limited average SNR. It is concluded from Fig. 16 that precoding exhibits superior BER improvement for low-order QAM modulation format due to its larger Euclidean distance. We set the LP to 6 dBm in the following discussions.

We also investigate the different output signal Vpp from the AWG to further explore the effects of the nonlinear distortions induced by the EA and DML on the BER performance. The related results are given in Fig. 17. Since the minimum signal Vpp from the AWG is 500 mV, we use a fixed 3 dB attenuator

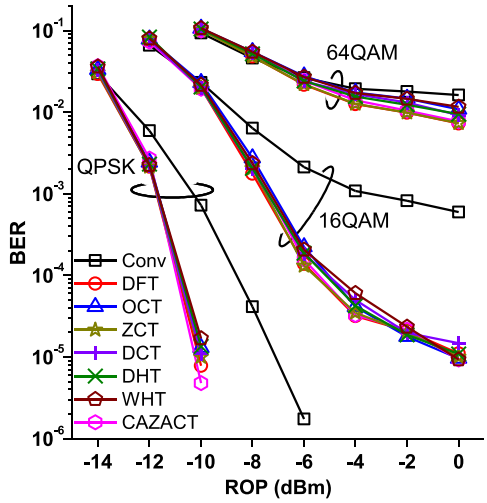

Fig. 19. The measured BER performance after 20 km transmission under different ROPs. (Vpp = 500 mV and LP = 6 dBm).

or two cascaded fixed 3-dB attenuators followed by the AWG with the signal Vpp of 500 mV to further reduce the signal Vpp. It indicates that the optimal signal Vpp is about 500 mV. For the small signal Vpp, the various noises (e.g., PD-induced noises) may be the dominant factor for the degraded BER performance. With the increase of signal Vpp, the BER performances for all three modulation formats are gradually degraded. It shows the complex-valued DFT/CAZACT/ZCT precoding techniques are more robust against these nonlinear distortions than the other precoding ones for 16 and 64QAM modulation formats. The experimental results agree with the results obtained by using nonlinear distortion models, as shown in Figs. 7 and 9. The BER performance is the noise-limited in small signal Vpp cases. Therefore, there is no obvious difference in the BER performance between OCT and the other precoded 16QAM DMT signals. The recovered 16QAM constellation diagrams and their EVM values are shown in Fig. 18. The slight improvements in the EVM performance, compared to the conventional signal, are mainly obtained from the PAPR reduction with precoding techniques.

The BER performance of the DMT signals after 20-km SMF transmission versus ROP is also investigated, as shown in Fig. 19. At the BER of 1e-3, the receiver sensitivities of QPSK and 16QAM-DMT transmission systems with precoding, in terms of ROP, can be improved by 1.4 and 4 dB, respectively, compared to the conventional DMT ones. The error floor at the high ROPs higher than −6 dBm is mainly due to that the PD is close to saturation. Noise limitation is the main reason for the slight improvement in BER performance of the 64QAM-DMT signals. In view of BER performance improvement and implementation complexity, WHT precoding may be a good option for the unbalanced impairments compensation in the noise-limited optical DMT transmission system.

IX. Conclusion

In this work, the SNR balance and implementation complexity were theoretically analyzed and discussed for seven commonly used precoding techniques in detail. Without taking ISI/ICI into account, the four complex-valued precoding techniques, i.e., ZCT, DFT, CAZACT and OCT, and one real-valued precoding technique WHT can achieve the best SNR balance. In the view of hardware implementation, no multipliers but only additions are required for WHT precoding; therefore, it has the lowest implementation complexity. And OCT precoding has the highest implementation complexity. We comparably investigated these precoding techniques in terms of PAPR reduction and nonlinear distortion tolerance by numerical simulations. It showed that three complex-valued precoding techniques (ZCT, DFT, and CAZACT) could achieve better PAPR reduction than the other three real-valued precoding techniques (DCT, DHT, and WHT) for different QAM modulation formats. Up to 3.7 dB PAPR reduction can be obtained by using ZCT precoding with QPSK modulation. However, less PAPR reduction is observed for higher-order modulation formats. And OCT precoding cannot reduce PAPR. With higher PAPR reduction, more improvements in EVM performance can be obtained under both the peak clipping and SSPA models. It was indicated that the precoded QPSK-DMT signals benefited from high PAPR reduction and outperformed the precoded ones with less or without PAPR reduction as well as the conventional one in the distortion-limited case. But the precoded 16/64QAM-DMT signals are more sensitive to nonlinear distortions and provide minor BER improvement or even may degrade the BER, compared to the OCT precoded and the conventional ones.

The estimated SNR distributions after decoding agree well with the theoretical ones. In the ISI-limited scenario, OCT precoding can achieve the best SNR balance and obtain the best BER performance. Besides, the SNR balance and the BER performance of the precoded DMT signals can be enhanced by the simple TSPA method in the presence of the ISI induced by channel low-pass filtering or/and SCPO. In the noise-limited case, the unbalanced impairments can be well compensated by every precoding technique. And all precoding techniques exhibited a similar improvement in BER performance.

Finally, the proof-of-concept experimental demonstrations are also performed in a short-reach DML-based DMT transmission system. Under the average power constraint, the unbalance impairments caused by the imperfect frequency response of the DAC and DML and CD-induced power fading were well compensated. And the receiver sensitivities of QPSK- and 16QAM-DMT were improved by 1.4 and 4 dB, respectively. A similar improvement in BER performance can be observed for these precoding techniques. Considering both the BER performance improvement and implementation complexity, WHT precoding may be a good option to compensate unbalanced impairments in the noise-limited optical DMT transmission system.

References

[1] T. Takahara *et al.*, "Discrete multi-tone for 100 Gb/s optical access networks," in *Proc. Opt. Fiber Commun. Conf. Exhib.*, 2014, Paper M2I.1.

[2] C. Qin, V. Houtsma, D. Van Veen, J. Lee, H. Chow, and P. Vetter, "40 Gbps PON with 23 dB power budget using 10 Gbps optics and DMT," in *Proc. Opt. Fiber Commun. Conf. Exhib.*, 2017, Paper M3H.5.

[3] A. Dochhan, H. Grießer, M. Eiselt, and J. Elbers, "Flexible bandwidth 448 Gb/s DMT transmission for next generation data center interconnects," in *Proc. Eur. Conf. Opt. Commun.*, 2014, Paper P.4.10.

[4] F. Li, J. Yu, Z. Cao, J. Zhang, M. Chen, and X. Li, "Experimental demonstration of four-channel WDM 560 Gbit/s 128QAM-DMT using IM/DD for 2-km optical interconnect," *J. Lightw. Technol.*, vol. 35, no. 4, pp. 941–948, Feb. 2017.

[5] F. Hu *et al.*, "20.09-Gbit/s underwater WDM-VLC transmission based on a single Si/GaAs-substrate multichromatic LED array chip," in *Proc. Opt. Fiber Commun. Conf. Exhib.*, 2020, Paper M3I.4.

[6] H. Qian, S. Cai, S. Yao, T. Zhou, Y. Yang, and X. Wang, "On the benefit of DMT modulation in nonlinear VLC systems," *Opt. Express*, vol. 23, no. 3, pp. 2618–2632, 2015.

[7] Y. Benlachtar *et al.*, "Generation of optical OFDM signals using 21.4 GS/s real time digital signal processing," *Opt. Express*, vol. 17, no. 29, pp. 17658–17668, 2009.

[8] X. Xiao, F. Li, J. Yu, Y. Xia, and Y. Chen, "Real-time demonstration of 100 Gbps class dual-carrier DDO-16QAM-DMT transmission with directly modulated laser," in *Proc. Opt. Fiber Commun. Conf. Exhib.*, 2014, Paper M2E.6.

[9] M. Chen, J. He, Q. Fan, Z. Dong, and L. Chen, "Experimental demonstration of real-time high-level QAM-encoded direct-detection optical OFDM systems," *J. Lightw. Technol.*, vol. 33, no. 22, pp. 4632–4639, Nov. 2015.

[10] J. Zhang *et al.*, "Stage-dependent DSP operation range clipping-induced bit resolution reductions of full parallel 64-point FFTs incorporated in FPGA-based optical OFDM receivers," *J. Lightw. Technol.*, vol. 34, no. 16, pp. 3752–3760, Aug. 2016.

[11] M. Chen, P. Zou, L. Zhang, and N. Chi, "Demonstration of a 2.34 Gbit/s real-time single silicon-substrate blue LED-based underwater VLC system," *IEEE Photon. J.*, vol. 12, no. 1, Feb. 2020, Art. no. 7900211.

[12] H. Dar-Zu *et al.*, "2.1-Tb/s/km OFDM long-reach PON transmission using a cost-effective electro-absorption modulator," in *Proc. Opt. Fiber Commun. Conf. Exhib.*, 2011, Paper OMG2.

[13] Z. Cao, G. Wen, F. Li, Q. Shu, J. Yu, and L. Chen, "Unbalanced impairments compensation for low cost direct detection OFDM-PON systems," *Opt. Commun.*, vol. 310, pp. 35–41, 2014.

[14] D. Zou *et al.*, "Comparison of null-subcarriers reservation and adaptive notch filter for narrowband interference cancellation in intra-data center interconnect with DMT signal transmission," *Opt. Express*, vol. 27, no. 4, pp. 5696–5702, 2019.

[15] L. Peng, M. Hélard, and S. Haese, "On bit-loading for discrete multi-tone transmission over short range POF systems," *J. Lightw. Technol.*, vol. 31, no. 24, pp. 4155–4165, Dec. 2013.

[16] C. Li, R. Hu, Q. Yang, M. Luo, W. Li, and S. Yu, "Fading-free transmission of 124-Gb/s PDM-DMT signal over 100-km SSMF using digital carrier regeneration," *Opt. Express*, vol. 24, no. 2, pp. 817–824, 2016.

[17] Y. Gao, J. Yu, J. Xiao, Z. Cao, F. Li, and L. Chen, "Direct-detection optical OFDM transmission system with pre-emphasis technique," *J. Lightw. Technol.*, vol. 29, no. 17, pp. 2138–2145, Jul. 2011.

[18] S. Karabetsos, E. Pikasis, T. Nikas, A. Nassiopoulos, and D. Syvridis, "DFT-spread DMT modulation for 1-Gb/s transmission rate over 100 m of 1-mm SI-POF," *IEEE Photon. Technol. Lett.*, vol. 24, no. 10, pp. 836–838, May 2012.

[19] T. Truong, M. Arzel, H. Lin, B. Jahan and M. Jézéquel, "DFT precoded OFDM—An alternative candidate for next generation PONs," *J. Lightw. Technol.*, vol. 32, no. 6, pp. 1228–1238, Mar. 2014.

[20] F. Li, J. Yu, Y. Fang, Z. Dong, X. Li, and L. Chen, "Demonstration of DFT-spread 256QAM-OFDM signal transmission with cost-effective directly modulated laser," *Opt. Express*, vol. 22, no. 7, pp. 8742–8748, 2014.

[21] F. Li, X. Li, L. Chen, Y. Xia, C. Ge, and Y. Chen, "High-level QAM OFDM system using DML for low-cost short reach optical communications," *IEEE Photon. Technol. Lett.*, vol. 26, no. 9, pp. 941–944, May 2014.

[22] F. Li, X. Li, J. Zhang, and J. Yu, "Transmission of 100-Gb/s VSB DFT-spread DMT signal in short-reach optical communication systems," *IEEE Photon. J.*, vol. 7, no. 5, Oct. 2015, Art. no. 7904307.

[23] Z. Feng *et al.*, "Performance-enhanced direct detection optical OFDM transmission with CAZAC equalization," *IEEE Photon. Technol. Lett.*, vol. 27, no. 14, pp. 1507–1510, Jul. 2015.

[24] Z. Feng *et al.*, "Dispersion-tolerant DDO-OFDM system and simplified adaptive modulation scheme using CAZAC precoding," *J. Lightw. Technol.*, vol. 34, no. 11, pp. 2743–2751, Jun. 2016.

[25] M. Chen *et al.*, "Experimental demonstration of an IFFT/FFT size efficient DFT-spread OFDM for short reach optical transmission systems," *J. Lightw. Technol.*, vol. 34, no. 9, pp. 2100–2105, May 2016.

[26] Y. Hong, X. Guan, L. Chen, and J. Zhao, "Experimental demonstration of an OCT-based precoding scheme for visible light communications," in *Proc. Opt. Fiber Commun. Conf. Exhib.*, 2016, Paper M3A.6.

[27] X. Chen, Z. Feng, M. Tang, S. Fu, and D. Liu, "Performance enhanced DDO-OFDM system with adaptively partitioned precoding and single sideband modulation," *Opt. Express*, vol. 25, no. 19, pp. 23093–23108, 2017.

[28] T. Jiang *et al.*, "Investigation of DC-biased optical OFDM with precoding matrix for visible light communications: Theory, simulations, and experiments," *IEEE Photon. J.*, vol. 10, no. 5, Oct. 2018, Art. no. 7906916.

[29] Y. Hong, L. Chen, and J. Zhao, "Performance-enhanced gigabit/s MIMO-OFDM visible light communications using CSI-free/dependent precoding techniques," *Opt. Express*, vol. 27, no. 9, pp. 12806–12816, 2019.

[30] J. Zhao, Y. Hong and L. Chen, "Discrete-circulant-transform spread OFDM for bandwidth-limited VLC systems," *J. Lightw. Technol.*, vol. 37, no. 20, pp. 5340–5353, Oct. 2019.

[31] R. Deng, J. He, M. Chen, and Y. Zhou, "Experimental demonstration of a real-time gigabit OFDM-VLC system with a cost-efficient precoding scheme," *Opt. Commun.*, vol. 423, pp. 69–73, 2018.

[32] J. Ma, M. Chen, K. Wu, and J. He, "Performance enhancement of probabilistically shaped OFDM enabled by precoding technique in an IM-DD system," *J. Lightw. Technol.*, vol. 37, no. 24, pp. 6063–6071, Dec. 2019.

[33] J. Ma *et al.*, "Performance enhanced 256-QAM BIPCM-DMT system enabled by CAZAC precoding," *J. Lightw. Technol.*, vol. 38, no. 3, pp. 557–563, Feb. 2020.

[34] Ö. Bulakçı, M. Schuster, C. Bunge, and B. Spinnler, "Precoding based peak-to-average power ratio reduction for optical OFDM demonstrated on compatible single-sideband modulation with direct detection," in *Proc. Opt. Fiber Commun. Conf. Exhib.*, 2008, Paper JThA56.

[35] O. Bulakci, M. Schuster, C. Bunge, and B. Spinnler, "Reduced complexity precoding based peak-to-average power ratio reduction applied to optical direct-detection OFDM," in *Proc. Eur. Conf. Opt. Commun.*, 2008, Paper P.4.11.

[36] X. Ouyang, J. Jin, G. Jin, and Z. Wang, "Low complexity discrete Hartley transform precoded OFDM for peak power reduction," *Electron. Lett.*, vol. 48, no. 2, pp. 90–91, 2012.

[37] J. Armstrong, "OFDM for optical communications," *J. Lightw. Technol.*, vol. 27, no. 3, pp. 189–204, Feb. 2009.

[38] I. Baig and V. Jeoti, "A new ZCT precoded OFDM system with pulse shaping: PAPR analysis," in *Proc. IEEE Asia Pacific Conf. Circuits Syst.*, 2010, pp. 1131–1134.

[39] J. H. van Lint and R. M. Wilson, *A Course in Combinatorics*. Cambridge, U.K.: Cambridge Univ. Press, 2001.

[40] M. Vetterli and H. J. Nussbaumer, "Simple FFT and DCT algorithms with reduced number of operations," *Signal Process.*, vol. 6, pp. 267–278, 1984.

[41] H. Sorensen, D. Jones, C. Burrus, and M. Heideman, "On computing the discrete Hartley transform," *IEEE Trans. Acoust., Speech, Signal Process.*, vol. ASSP-33, no. 5, pp. 1231–1238, Oct. 1985.

[42] A. Cann, "Nonlinearity model with variable knee sharpness," *IEEE Trans. Aerosp. Electron. Syst.*, vol. AES-16, no. 6, pp. 874–877, Nov. 1980.

[43] S. Amiralizadeh, A. Nguyen, and L. Rusch, "Modeling and compensation of transmitter nonlinearity in coherent optical OFDM," *Opt. Express*, vol. 23, no. 20, pp. 26192–26207, 2015.

[44] M. Chen, J. He, Z. Cao, J. Tang, L. Chen, and X. Wu, "Symbol synchronization and sampling frequency synchronization techniques in real-time DDO-OFDM systems," *Opt. Commun.*, vol. 326, pp. 80–87, 2014.

[45] X. Liu and F. Buchali, "Intra-symbol frequency-domain averaging based channel estimation for coherent optical OFDM," *Opt. Express*, vol. 16, no. 26, pp. 21944–21957, 2008.

[46] R. I. Laming, M. N. Zervas, and D. N. Payne, "Erbium-doped fibre amplifier with 54 dB gain and 3.1 dB noise figure," *IEEE Photon. Technol. Lett.*, vol. 4, no. 12, pp. 1345–1347, Dec. 1992.

[47] I. Tomkos, B. Hallock, I. Roudas, R. Hesse, A. Boskovic, and R. Vodhanel, "Transmission of 1550 nm 10 Gb/s directly modulated signal over 100 km of negative dispersion fiber without any dispersion compensation," in *Proc. Opt. Fiber Commun. Conf. Exhib.*, 2001, Paper TuU6-1.

[48] C. C. Wei, "Small-signal analysis of OOFDM signal transmission with directly modulated laser and direct detection," *Opt. Lett.*, vol. 36, no. 2, pp. 151–153, 2011.